Geophysical Journal International

Geophys. J. Int. (2014) **199,** 956–967 doi: 10.1093/gji/ggu306

GJI Mineral physics, rheology, heat flow and volcanology

In situ frictional properties of San Andreas Fault gouge at SAFOD

C. G. Coble,* M. E. French, F. M. Chester, J. S. Chester and H. Kitajima†

Center for Tectonophysics, Department of Geology & Geophysics, Texas A&M University, College Station, TX 77843-3115, *USA.*
E-mail: melodie.french@tamu.edu

Accepted 2014 August 4. Received 2014 July 26; in original form 2014 May 1

SUMMARY

Along the central segment of the San Andreas Fault (SAF) near Parkfield, California, displacement occurs by a combination of aseismic creep and micro-earthquake slip. To constrain the strength and parametrize a constitutive relation for the creeping behaviour of the central segment of the SAF, we conducted friction experiments on clay-rich gouge retrieved by coring the Central Deforming Zone (CDZ) of the SAF at 2.7 km vertical depth. The gouge was flaked rather than powdered to preserve the natural scaly microfabric, and formed into 2-mm-thick layers that were sheared using a triaxial deformation apparatus. Experiments were conducted at *in situ* effective normal stress (100 MPa), pore pressure (25 MPa) and temperature (80–120 °C) conditions using brine pore fluid with the ionic composition of the *in situ* formation fluid. Velocity-stepping (0.006–0.6 μm s^{-1}) and temperature-stepping experiments were conducted on brine-saturated gouge, and slide-hold-slide experiments were conducted on brine-saturated and room-dry gouge. Results are used to quantify the effects of rate, state, temperature and pore fluid on the strength of the CDZ gouge. We find that the gouge is extremely weak ($\mu < 0.13$) and rate-strengthening, consistent with findings of previous studies on the CDZ gouge. We also find that, in a rate and state friction framework, slip history has a negligible effect on strength ($b \approx 0$) under both saturated and dry conditions. The CDZ gouge is temperature-weakening from 80 to 120 °C and weakens 17 per cent when saturated with brine compared to room-dry conditions. Employing the laboratory-derived friction constitutive parameters, and including the temperature weakening and the strain-rate strengthening effects, we determine an approximate *in situ* friction coefficient of $\mu \approx 0.11$. For $\mu \approx 0.11$, aseismic creep under normal pore fluid conditions is permitted for angles up to 79° between the maximum horizontal stress and the plane of the SAF, consistent with nearby stress orientation measurements.

Key words: Geomechanics; Creep and deformation; Friction; Fault zone Rheology.

1 INTRODUCTION

Abundant evidence suggests that the locked and creeping segments of the San Andreas Fault (SAF) are weak in both a relative and absolute sense. Borehole breakouts and drilling-induced tensile fractures in the San Andreas Fault Observatory at Depth (SAFOD), stress orientations from inversion of earthquake focal mechanisms, and thrust faults and anticlinal axes that strike subparallel to the SAF, indicate that the maximum horizontal compressive stress, $S_{H,}$ is oriented between 65° and 85° to the SAF consistent with a low apparent coefficient of sliding friction, μ_a (Mount & Suppe 1987; Zoback *et al.* 1987; Provost & Houston 2001; Hickman & Zoback 2004). Furthermore, evaluation of heat flow data from along the fault using fluid flow and heat transport model analyses indicates that frictional heating is significantly lower than predicted if μ_a during slip on the SAF is as large as 0.5, and that the fault is weak in an absolute sense (Brune *et al.* 1969; Lachenbruch & Sass 1980; Provost & Houston 2001; Fulton *et al.* 2004, 2009; Williams *et al.* 2004; Fulton & Saffer 2009a,b).

Hypotheses proposed to explain the low apparent coefficient of friction along the central creeping section of the SAF include: (1) the presence of intrinsically weak minerals (e.g. smectite and talc) that allow frictional slip at a low resolved shear stress (Moore & Rymer 2007; Lockner *et al.* 2011; Carpenter *et al.* 2012) and that often develop natural foliations defined by strong mineral fabrics (e.g. mica folia; Collettini *et al.* 2009; Niemeijer *et al.* 2010; Schleicher *et al.* 2010; Moore & Lockner 2011), (2) the condition of sustained elevated pore fluid pressure within the fault core, which lowers the effective normal stress on the fault and allows slip at a low resolved shear stress (Lachenbruch 1980; Rice 1992; Fulton *et al.* 2009; Fulton & Saffer 2009b) and (3) deformation by pressure-independent mechanisms, such as dissolution-aided slip

*Now at: Hess Corporation, Houston, TX, USA.
†Now at: Institute of Earthquake and Volcano Geology, Geological Survey of Japan, Ibabraki, Japan.

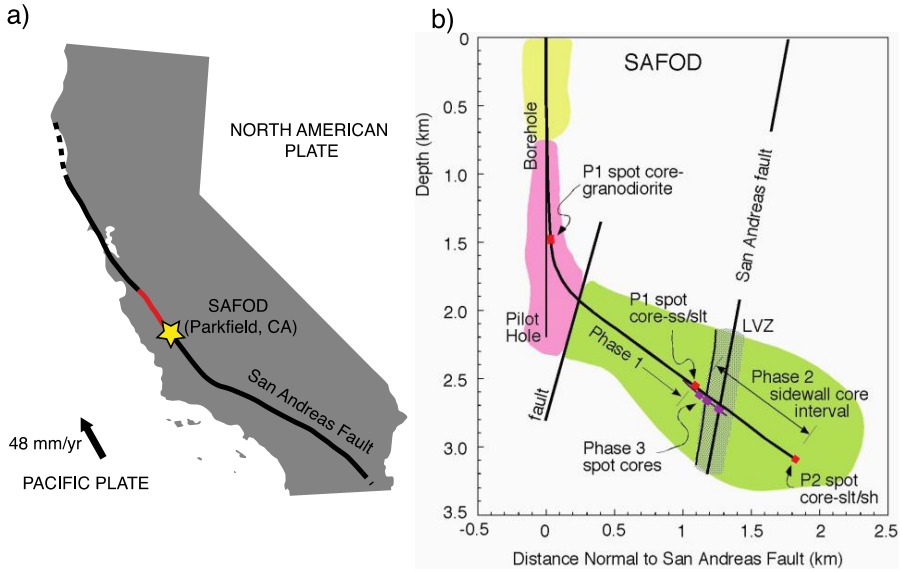

Figure 1. (a) The SAFOD site (star) is located along the aseismic creeping section of the SAF (red) in central California near the town of Parkfield. The northern and southern sections of the SAF (black) are locked and slip along these sections of the fault occurs by large magnitude earthquakes. (b) From *Chester et al.* 2007. Initial drilling of the SAFOD borehole took place on the west side of the fault. The borehole was then deviated and crossed the SAF at 2.7 km true vertical depth. The major rock types cut by the borehole are indicated by yellow, pink and green shading for Quaternary/Tertiary sedimentary rocks, Salinian granitic rocks, and sedimentary rock comprised of sandstones, siltstones and shales, respectively. The SAF gouge used in this study was taken from the Phase 3 spot cores.

and dislocation glide in phyllosilicates (Rutter & Mainprice 1978; Bos *et al.* 2000; Gratier *et al.* 2011; Moore & Lockner 2013).

To test hypotheses for the cause of fault weakening mechanisms, experiments have been conducted on exhumed fault rocks (Numelin *et al.* 2007; Collettini *et al.* 2009; Smith & Faulkner 2010), and on artificial gouge containing representative minerals found in natural faults (Morrow *et al.* 2000; Saffer & Marone 2003; Moore & Lockner 2004, 2008; Ikari *et al.* 2009; Niemeijer *et al.* 2010; Tembe *et al.* 2010). Several recent continental and ocean drilling projects make it possible to measure the strength of fault rocks taken from an active fault at seismic depths (e.g. Tembe *et al.* 2006; Morrow *et al.* 2007; Mizoguchi *et al.* 2009; Sone & Shimamoto 2009; Boulton *et al.* 2014), including several studies that explore the behaviour of natural fault gouge taken from the actively creeping zones of the SAF at ~3 km depth in the SAFOD borehole (Lockner *et al.* 2011; Carpenter *et al.* 2012; French *et al.* 2014).

SAFOD is located within the central creeping segment of the SAF, a few kilometres northwest of the transition with the southern locked segment (Fig. 1). In the vicinity of SAFOD, fault displacement occurs through a combination of aseismic creep and repeating micro-earthquakes. The borehole intersects two actively creeping traces of the SAF, the Southwest Deforming Zone (SDZ) at 3192 m measured depth (MD) and the Central Deforming Zone (CDZ) at 3302 m MD (Zoback *et al.* 2010). The measured depths correspond to true vertical depths of 2620 and 2675 m, respectively. The creeping zones are composed of dark greyish-black, ultrafine-grain, foliated fault gouge that contains clasts of serpentinite, siltstone and fine-grained sandstone (Bradbury *et al.* 2011; Holdsworth *et al.* 2011; Hadizadeh *et al.* 2012).

Recent measurements of anomalously low frictional strength ($\mu < 0.2$) in gouge recovered from the CDZ indicate that the creeping segment of the SAF is weak in an absolute sense (Lockner *et al.* 2011; Carpenter *et al.* 2012). Friction experiments using the CDZ gouge show strengthening with increasing velocity, a property that implies that the creeping segment of the SAF is inherently seismically stable (Coble 2010; Lockner *et al.* 2011; Carpenter *et al.* 2012). The experiments were conducted on powdered CDZ gouge samples (Lockner *et al.* 2011; Carpenter *et al.* 2012) or intact wafers (Carpenter *et al.* 2012) at high normal stresses (50–200 MPa), brine-saturated conditions, and at room temperature. Lockner *et al.* (2011) show that the intrinsically low strength of the CDZ gouge is consistent with measurements of the orientation of S_H at high-angles to the SAF within the fault damage zone because stresses rotate within the weak CDZ gouge (e.g. Rice 1992). Using this analysis, they estimate that the effective normal stress at 2.7 km depth is ~122 MPa.

The purpose of this study is to expand our understanding of the mechanical properties of the aseismic creeping section of the SAF by quantifying the effects of temperature, strain rate, and slip history on the frictional strength of the CDZ gouge. To achieve this goal we conducted low-speed shear experiments on gently flaked CDZ gouge at conditions of temperature, stress and pore-fluid chemistry that simulate *in situ* seismogenic depth conditions. Using these data we present the constitutive relationship for the CDZ gouge under the most realistic *in situ* conditions published to date.

We describe the velocity, slip history and temperature dependencies by fitting the experimental data to the temperature-dependent rate and state friction model (Chester 1994). This constitutive relation is adapted from the ageing rate and state friction law to incorporate the effects of temperature (Dieterich 1978). The friction coefficient, μ, at slip velocity, V and temperature, T, is

$$\mu = \mu^* + a\left[\ln\left(\frac{V}{V^*}\right) + \frac{E_a}{R}\left(\frac{1}{T} - \frac{1}{T^*}\right)\right] + b\ln\left(\frac{V^*\theta}{D_c}\right) \quad (1a)$$

$$\frac{d\theta}{dt} = 1 - \left(\frac{V\theta}{D_c}\right) - \frac{E_b}{R}\left(\frac{1}{T} - \frac{1}{T^*}\right), \quad (1b)$$

where a is the constant describing the direct effect, b describes the evolution effect, θ is the state variable, D_c is the slip weakening distance, E_a and E_b are the activation energies of the mechanisms responsible for the direct and evolution effects, respectively, and R is the ideal gas constant. Starred parameters indicate values at reference conditions. The steady-state velocity dependence is

$$\left[\frac{d\mu}{d(\ln V)}\right]_T = a - b \tag{2a}$$

and the steady-state temperature dependence is

$$\left[\frac{d\mu}{d(1/T)}\right]_V = (aE_a - bE_b)/R \tag{2b}$$

Friction experiments on the CDZ gouge were conducted at an effective normal stress of 100 MPa, close to the 122 MPa effective normal stress determined by Lockner *et al.* (2011), and pore fluid pressure of 25 MPa. A combination of velocity-stepping, slide-hold-slide and temperature-stepping experiments were conducted and analysed to parametrize the constitutive relation given by eqs (1a) and (1b). Velocity-stepping at shear slip rates of 0.6, 0.06 and 0.006 μm s^{-1} and slide-hold-slide experiments at 0.06 μm s^{-1} show that the CDZ gouge is steady-state velocity strengthening, exhibits negligible healing, and has an evolution effect that is very small ($b \approx 0$). Temperature-stepping experiments at 80, 100, and 120 °C show the strength of the CDZ gouge decreases with increasing temperature with all other conditions constant (temperature-weakening), which is consistent with velocity-strengthening behaviour if both dependencies reflect the same mechanisms (Chester 1994).

2 METHODS

2.1 Sample composition and preparation

The CDZ gouge used in this study is from Hole G, Core Run 4, Section 4, 9 cm from the top of the section. The gouge was gently disaggregated to particle diameters of about 844 μm; the large particle size was used to preserve the natural microfabric and porphyroclasts within the gouge. The brine used as the pore fluid in these experiments has the same composition as the formation fluid recovered from the SAFOD borehole at a measured depth of 3594 m; the concentration of the primary ionic components of the formation fluid is 15.7 g L^{-1} of Cl, 5.72 g L^{-1} of Na, 3.62 g L^{-1} Ca and 0.22 g L^{-1} of K (Kharaka & Thordsen, personal communication, 2007).

2.2 Triaxial shear experiments

Triaxial shear experiments were conducted by placing 2.65 g of flaked room-dry CDZ gouge between a sawcut in a cylindrical Coconino Sandstone forcing block, 19.05 mm in diameter. The sawcut was oriented at 35° to the shortening direction and long axis of the cylinder (Fig. 2). The Coconino Sandstone porosity (~13.7–14.8 per cent) and high permeability (~4.2 × 10^{-15}–2.2 × 10^{-14} m^2) facilitate transmission of the pore fluid to the gouge layer and maintenance of the desired pore fluid pressure. The 35° pre-cut surfaces were wet-sanded with 220 grit silicon carbide sand paper to produce uniform and repeatable roughness.

An inner silver foil and outer Teflon jacket sealed the sample; the foil reduces diffusion of pore fluid through the Teflon jacket and out of the sample. Samples deformed with brine pore fluid were saturated in a vacuum chamber for approximately 12 hr before

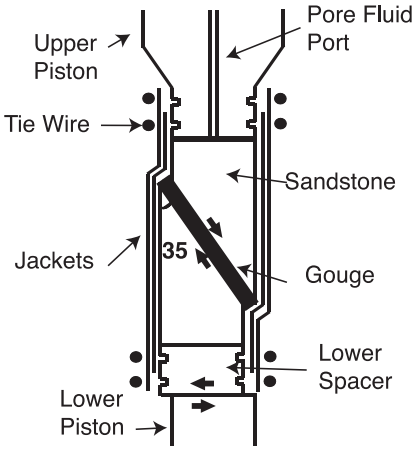

Figure 2. Sample assembly and jacketing configuration.

applying the outer jacket and sealing the assembly with tie-wires. Samples were allowed to equilibrate at temperature and pressure for 24 hr prior to sliding. When compacted to 100 MPa effective confining pressure, the brine-saturated gouge layer is ~2 mm thick.

Experiments were conducted in a gear-driven, variable strain-rate, triaxial rock deformation apparatus using silicone fluid as the confining medium (Heard 1963; Chester 1988; Fig. 2). The apparatus incorporates an internal force gauge for sensitive force measurements that does not require a correction for seal friction, an external furnace for stable temperatures with temperature variations along the sample that are less than 1 per cent of the reported temperature, an independently controlled pore fluid pressure system incorporating a volumeter used to measure pore volume changes in the sample, and corrosion-resistant stainless steel and inconel plumbing to minimize reactions with pore fluids.

All experiments were conducted at constant effective normal stress by manually maintaining a constant pore fluid pressure and adjusting the confining pressure during shearing. Adjustment of the confining pressure to maintain constant normal stress is standard operating procedure during friction tests in the triaxial configuration, because normal stress is coupled to axial force, which evolves with changes in gouge strength. Real-time monitoring of experimental conditions was used to calculate the effective normal stress, which allows for the confining pressure to be adjusted appropriately. The calculation of effective normal stress also takes into account the strength of the sealing jacket. Parameters recorded during the experiment were elapsed time, confining pressure (accuracy of 0.07 MPa), pore fluid pressure, P_p (with an error of less than 0.02 MPa), displaced pore fluid pressure volume (accurate to 0.02 cc), differential axial force (accurate to 15 lbs), axial displacement (accurate to 5 μm), and temperature (with an error of less than 1 °C).

CDZ gouge experiments were performed at a constant effective normal stress of 100 MPa, pore fluid pressure of 25 MPa (except for the dry sample), and at 100 °C (with the exception of the temperature stepping experiment) to best simulate the conditions at 2.7 km depth in the fault zone (Table 1). One room-dry sample was deformed at 100 °C; like the brine-saturated samples, this sample was allowed to equilibrate at temperature for 24 hr prior to sliding.

The steady-state rate-dependence of the CDZ gouge (a–b, eq. 2a) is determined from velocity-stepping tests conducted from 0.006 to 0.6 μm s^{-1}. Step changes consist of an increase or decrease in velocity by one or two orders of magnitude during steady-state sliding. The friction parameters a, b and D_c were determined using

Table 1. Matrix of shear experiments on gouge layers.

Gouge material	Experiment ID	Test type	Pore fluid	T (°C)	Shear displ. rate (μm s^{-1})	Shear displ. (mm)
CDZ	SG1	SHS	Brine	100	0.6	4.25
CDZ	SG2	SHS	Brine	100	0.6	4.25
CDZ	SG3	SHS	Dry	100	0.6	4.25
CDZ	SG6	VS	Brine	100	0.6, 0.06, 0.006	4.25
CDZ	SG7	VS, TS	Brine	80, 100, 120	0.6, 0.06, 0.006	4.25

Notes: All experiments were conducted at 100 MPa effective normal stress. In brine saturated CDZ gouge pore fluid pressure was 25 MPa. T is temperature, SHS is slide-hold-slide, VS is velocity stepping, TS is temperature stepping.

inverse models of slide-hold-slide tests; holds were conducted in time increments of an order of magnitude and lasted between 1 and 10^5 s.

The steady-state temperature dependence of CDZ gouge (eq. 2b) was determined by stepping the temperature at 0.25 mm shear displacement intervals. The slowest displacement rate of 0.006 μm s^{-1} was employed to minimize the displacement while temperature and pore fluid pressure equilibrate during and following temperature steps. The sample was loaded and sheared at an initial temperature of 100 °C and was then stepped to 80, 100, 120 and 100 °C.

2.3 Inverse modelling of slide-hold-slide tests

Because the apparatus used to collect the data reported herein is relatively compliant, the evolution of stress following a velocity-step or a hold is significantly influenced by elastic deformation of the apparatus. It is, therefore, difficult to directly determine the friction parameters from the mechanical data. Accordingly, we employ a least-squares inverse model to objectively determine the parameters of the rate and state constitutive relation (eqs 1a and 1b) to estimate the magnitudes of the parameters a, b and D_c for brine-saturated and room-dry gouge during the slide-hold-slide tests. The inverse model fits the evolution of stress with time during the 'holds' and reloads with the rate- and state-friction relation, and the utility of this approach lies in the reduced dependence on the reloading behaviour.

The change in friction coefficient with time during the experiments is

$$\frac{\mathrm{d}\mu}{\mathrm{d}t} = k_\mu \left(\frac{V_{\mathrm{lp}}}{\cos\alpha} - V \right), \tag{3}$$

where k_μ is the elastic stiffness of the apparatus and sample in units of coefficient of friction per unit shear displacement, V_{lp} is the load point velocity, V is the velocity of the gouge layer parallel to the sawcut and α is the angle between the core axis and sawcut surface (35°). The constant k_μ can be determined from the total stiffness of the apparatus and sample ($k = k_{\mathrm{A}} + k_{\mathrm{S}}$) using the relation $k_\mu = k(\cos\alpha)[\sin(2\alpha)](1 - \mu\tan\alpha)^2/2AP_{\mathrm{ce}}$, where A is the cross sectional area of the cylinder corrected for shear offset, and P_{ce} is the effective confining pressure (Chester & Higgs 1992). For each experiment and model, the total stiffness, k, is that measured during the elastic loading and unloading portions of the experiment. From eq. (3) it is apparent that during steady state shearing ($\mathrm{d}\mu/\mathrm{d}t = 0$) $V_{\mathrm{lp}}/\cos\alpha = V$, and during the holds ($V_{\mathrm{lp}} = 0$) $\mathrm{d}\mu/\mathrm{d}t$ and V continuously decrease with time until shearing is resumed.

The evolution of the CDZ gouge strength with time is completely described by eqs (1a), (1b), and (3). We used a fourth order Runge–Kutta method to solve eqs (1a), (1b), and (3) for V and solved the system of eqs (1a) and (1b) for μ^*, a, b and D_c using the least-squares inverse model presented by Reinen & Weeks (1992). This procedure is consistent with published methods of determining the rate and state frictional properties of fault rock (Blanpied *et al.* 1998; Ikari *et al.* 2009).

Table 2. Matrix of experiments to determine jacket strength.

Experiment ID	P_c (MPa)	T (°C)	Shear displ. rate (μm s^{-1})	Shear displ. (mm)
ST-80–1	80, 60	100	0.6	4.0
ST-50–1	50, 70	100	0.6	4.0
ST-80–2	80	100	0.6	4.0

2.4 Jacket strength determination

Dedicated experiments are used to determine the strength of the jackets as a function of effective pressure and displacement, and the results are used to correct the mechanical data and accurately determine the coefficient of friction of the CDZ gouge. Jacket strength is determined using the same sample and jacketing configuration as the gouge experiments except (1) the cut cylinders are steel and the cut surfaces are ground to a surface roughness of 0.4 μm, (2) the inclined surface is lubricated with silicone fluid to reduce sliding friction and (3) pore fluids are not used. The steel cylinder is 18.54 mm in diameter, and experiments are conducted at a constant confining pressure (Table 2).

Jacket strength is determined following the analysis of mechanical data outlined by Chester (1994). The effective normal stress, σ_n^{e}, and shear stress, τ, across the pre-cut surface are given by

$$\sigma_n^{\mathrm{e}} = \left(P_{\mathrm{c}} - P_p\right) + \left[\left(\Delta F_t - \Delta F_j\right)\sin^2\alpha + \mu_{\mathrm{ls}}\Delta F_t\cos\alpha\sin\alpha\right]/A_{\mathrm{ls}} \tag{4a}$$

$$\tau = \left[\left(\Delta F_t - \Delta F_j\right)\cos\alpha\sin\alpha - \mu_{\mathrm{ls}}\Delta F_t\sin^2\alpha\right]/A_{\mathrm{ls}}, \tag{4b}$$

where P_{c} is the confining pressure, P_{p} is the pore fluid pressure, α is the angle between the pre-cut surface and the maximum principal stress (35°), ΔF_{t} is the differential force, ΔF_{j} is the differential force supported by the jackets, μ_{ls} is the coefficient of friction of the interface between the lower piston and lower spacer and A_{ls} is the cross-sectional area of the interface between the lower piston and lower spacer. From $\tau = \mu\sigma_n^{\mathrm{e}}$, where μ is the coefficient of friction of the 35° sliding interface, eqs (4a) and (4b) may be substituted to derive a single expression relating the three unknowns, μ, ΔF_{j} and μ_{ls}.

$$\mu = \frac{\tau}{\sigma_n^{\mathrm{e}}} = \frac{\left[(\Delta F_t - \Delta F_j)\cos\alpha\sin\alpha - \mu_{\mathrm{ls}}\Delta F_t\sin^2\alpha\right]}{(P_c - P_p) + \left[(\Delta F_t - \Delta F_j)\sin^2\alpha + \mu_{\mathrm{ls}}\Delta F_t\cos\alpha\sin\alpha\right]}. \tag{5}$$

The best-fitting values of μ and μ_{ls} were determined from a previous suite of jacket strength tests (Coble 2010), and ΔF_{j} is determined as a function of effective pressure and displacement.

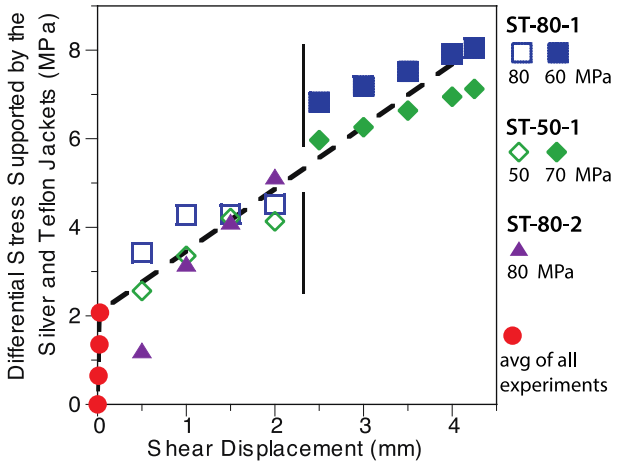

Figure 3. Plot of the differential stress supported by the silver foil and Teflon jacket at 100 °C as a function of shear displacement for confining pressures of 50, 60, 70 and 80 MPa. In some experiments the confining pressure was stepped up or down at displacements of approximately 2.3 mm. The jacket strength varies little with effective confining pressure. The average strength of jackets at all confining pressures tested are indicated by red symbols for shear displacements less than 0.02 mm. At greater shear displacement, jacket strength was calculated at shear displacement intervals of 0.5 mm. The jackets strengthen with shear displacement and are best described by separate functions for small displacements (<0.02 mm; eq. 6a) and large displacements (>0.02 mm) (eq. 6b).

The variation in strength caused by changes in confining pressure is less than the magnitude of sample-to-sample variation, thus it is assumed that jacket strength is independent of effective pressure (Fig. 3). This variation in the sample-to-sample strength introduces a maximum error of 1.5 MPa in the jacket correction; this is the largest source of uncertainty in our measurements of the absolute magnitude of gouge friction (μ^*). A bilinear relationship is needed to describe the strength of the jackets at small and large displacements. For small displacements

$$\Delta\sigma_j = 71.35d \tag{6a}$$

and for large displacements

$$\Delta\sigma_j = 1.41d + 2.05, \tag{6b}$$

where $\Delta\sigma_j$ is the differential stress supported by the silver and Teflon jackets in MPa and d is the shear displacement in mm.

3 RESULTS

3.1 Frictional strength of the SAFOD gouge

The strength of the CDZ gouge is $\mu \approx 0.13$ at 100 °C, which is similar to the strength of the CDZ gouge measured by Lockner *et al.* (2011) and Carpenter *et al.* (2012) (Fig. 4a). Comparison of experiments conducted on room-dry and brine-saturated CDZ gouge samples shows that the frictional strength is reduced 17 per cent by the presence of the pore fluid. The CDZ gouge compacts throughout shear deformation at a rate that is relatively constant with shear displacement (Fig. 4b).

3.2 Steady-state velocity dependence

Velocity-stepping experiments show that the steady-state velocity dependence of brine-saturated CDZ is positive, i.e. the CDZ gouge

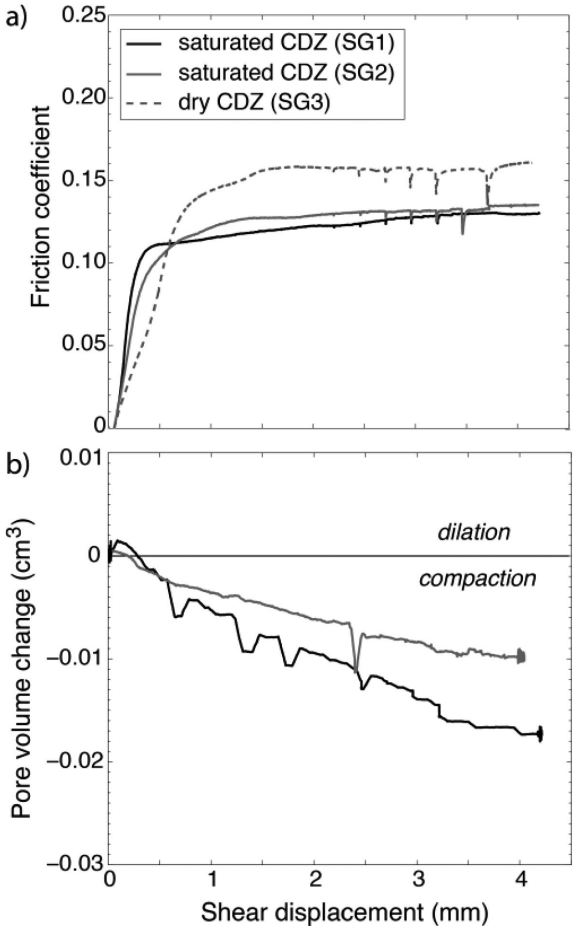

Figure 4. Results from experiments on brine-saturated and room-dry CDZ gouge. All experiments were conducted at 100 MPa effective normal stress, shear velocity of 0.6 μm s^{-1}, and 100 °C. (a) The evolution of friction coefficient with shear displacement. (b) The evolution of pore volume with shear displacement for saturated CDZ gouge. Pore volume changes were not measured for dry gouge. Positive and negative volume changes indicate dilation and compaction, respectively. Based on an approximately 2-mm-thick elliptical gouge layer, the total reduction in pore volume corresponds to compaction of 1–2 per cent in these experiments.

is velocity strengthening (Fig. 5). Measured values of $a - b$ (eq. 2a) range between 0.0005 and 0.0022 with an average and standard deviation of 0.0014 ± 0.0005 (Fig. 6). The velocity dependence is determined by the difference in the average coefficient of friction spanning the 0.25 mm preceding and succeeding the velocity step. There is no consistent trend in the magnitude of $a - b$ between samples or with either a step up or step down in velocity.

3.3 Transient frictional behaviour

The coefficient of friction of the CDZ gouge does not change significantly or systematically when sliding resumes following a hold, indicating negligible time-dependent healing over the time-scales tested (Figs 4a and 7). For time- or slip-dependent frictional processes, the gouge is expected to strengthen following a hold. The lack of significant healing, which was also observed at displacement rates three to four orders higher in magnitude by Carpenter *et al.* (2011) and Carpenter *et al.* (2012), suggests that in a rate and state friction framework, the magnitude of b is small.

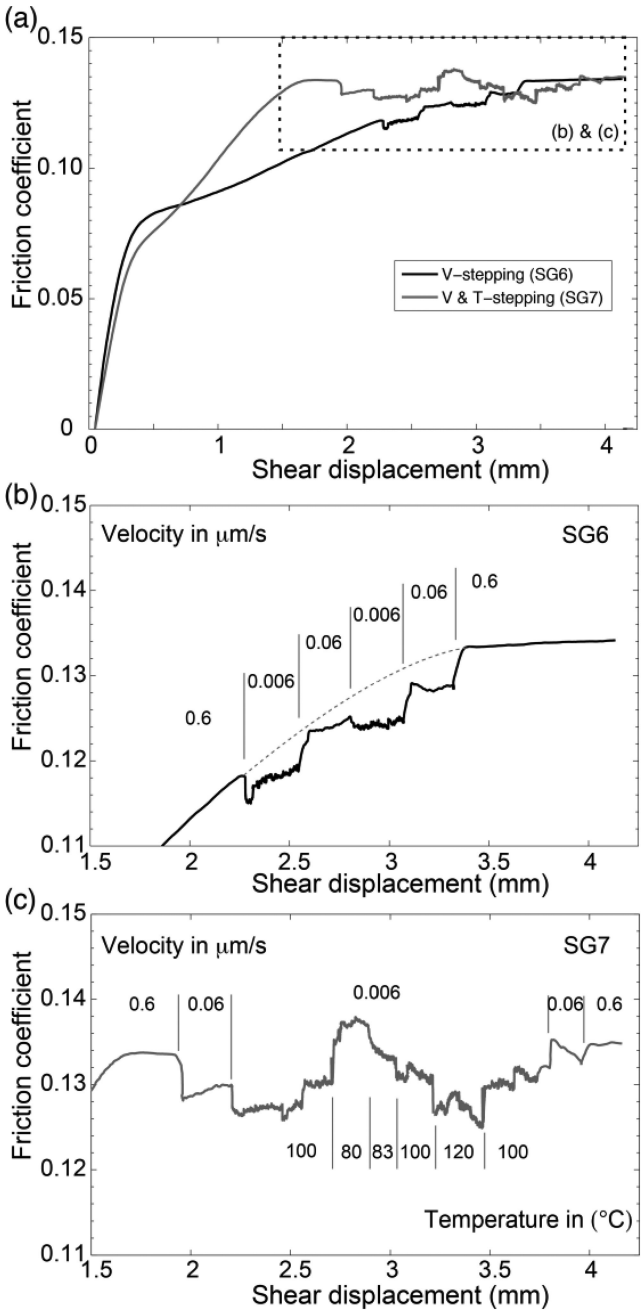

Figure 5. (a) The evolution of friction coefficient with shear displacement for velocity-stepping (SG6 and SG7) and temperature-stepping (SG7) experiments. The dashed box is the data range shown in (b) and (c). The analsed velocity- and temperature-stepping data are shown in Figs 6 and 9, respectively. Velocity and temperature-stepping tests were conducted after 2 mm displacement when the steady-state strength of the gouge is similar in the two experiments. Differences in the strain hardening behaviour most likely represent redistribution of the gouge between the sawcut surfaces. (b) Friction coefficient with shear displacement for velocity-stepping experiment SG6. The experimental conditions are 100 MPa effective normal stress and 100 °C. Velocity was stepped between 0.006, 0.06 and 0.6 μm s^{-1}. (c) Friction coefficient with shear displacement for velocity-stepping and temperature stepping experiment SG7. The experimental conditions are 100 MPa effective normal stress. Velocity was stepped between 0.006, 0.06 and 0.6 μm s^{-1} at a constant temperature of 100 °C. Temperature was stepped between 80, 100 and 120 °C at a constant velocity of 0.006 μm s^{-1}.

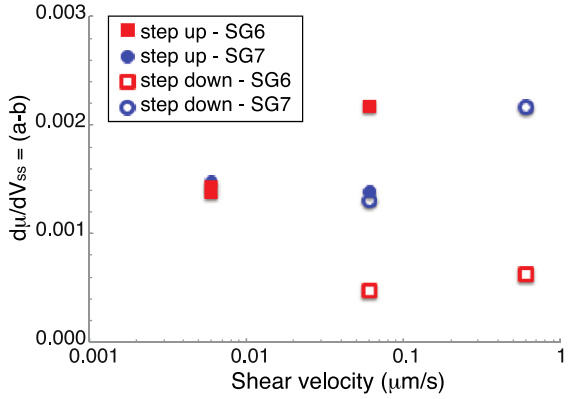

Figure 6. Steady state velocity dependence parameter ($a - b$) versus shear velocity for experiments SG6 and SG7 (Fig. 5). Both tests were conducted at 100 °C and 100 MPa effective normal stress. The $a - b$ value is always positive indicating velocity-strengthening behaviour and the average and standard deviation are: 0.0014 ± 0.0005. The $a - b$ measurements have a similar range of magnitudes for each velocity tested.

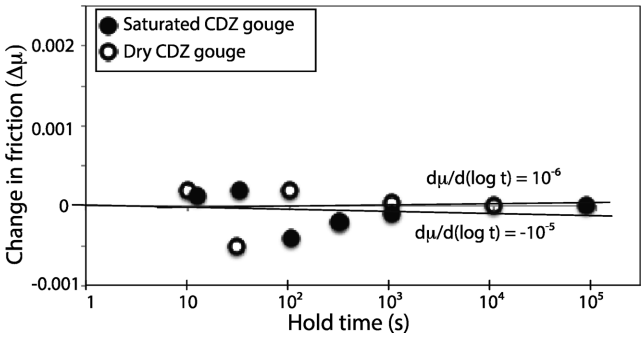

Figure 7. The difference between the peak friction coefficient following a hold and steady state friction coefficient preceding the hold (Δμ) as a function of hold time for the CDZ gouge experiments shown in Fig. 4. All experiments were conducted at 100 MPa effective normal stress, shear velocity of 0.6 μm s^{-1}, and 100 °C. Neither room-dry nor brine-saturated gouge strengthens measurably.

The rate and state friction parameters estimated from inverse models of slide-hold-slide tests confirm that brine-saturated CDZ gouge is velocity-strengthening and the magnitude of b is small ($b \approx 0$; Fig. 8). For brine-saturated gouge, $a - b$ varies from 0.0006 to 0.0028 with an average of 0.0014, the same as determined from velocity-stepping experiments. Inverse model estimates for the magnitude of a range from 0.0008 to 0.0014 with an average $a_{avg} = 0.0011$, and estimates for b range from −0.0014 to 0.0002 with an average $b_{avg} = -0.0003$ ($b_{avg} = 0$ if the longest hold lasting 1 day is excluded). The results of all of the tests can be reasonably well fit with the model $b = 0$ (Fig. 8).

The magnitude of steady state velocity-strengthening in the CDZ gouge, $a - b = 0.0014 \pm 0.005$, is within the range reported by Lockner *et al.* (2011) and Carpenter *et al.* (2012), and is similar to values from several other studies on clay rich gouge (Saffer & Marone 2003; Tembe *et al.* 2006; Morrow *et al.* 2007; Moore & Lockner 2008; Carpenter *et al.* 2009, 2011; Ikari *et al.* 2009; Tembe *et al.* 2010). Clay-rich gouges, such as the CDZ gouge, have very low permeability (10^{-18} to 10^{-21} m^2; Morrow *et al.* 1984; Faulkner & Rutter 2003; Takahashi *et al.* 2007; Ikari *et al.* 2009) and at the fastest shear velocities, the pore fluid pressure does not equilibrate. As a result, there could be over or under pressurization caused by

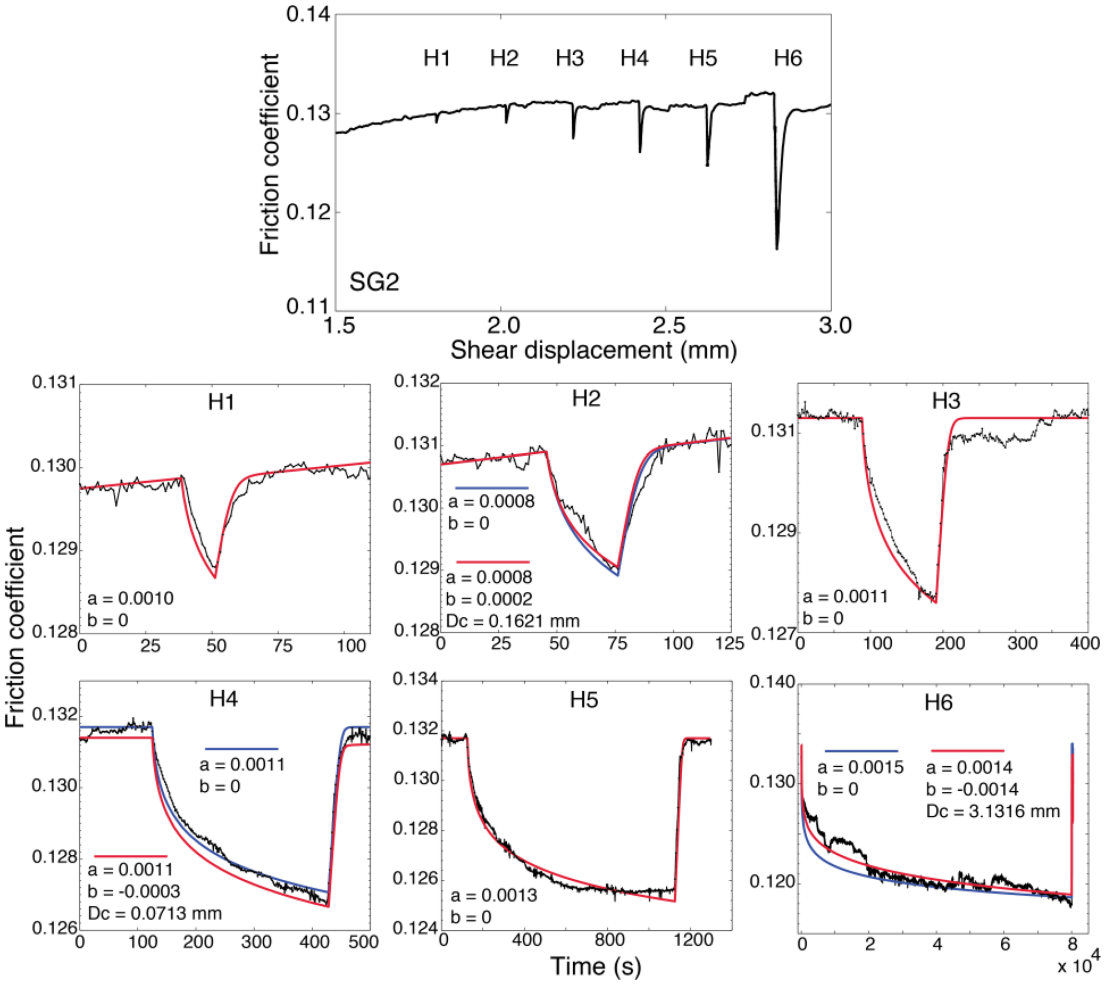

Figure 8. Top panel: an expanded view of the evolution of friction coefficient with displacement for the slide-hold-slide experiment SG2 also shown in Fig. 4. The sample is brine-saturated CDZ gouge deformed at 100 MPa effective normal stress, 100 °C and 0.6 μm s^{-1}. Bottom panels: the experimentally determined evolution of friction coefficient with time during the six holds (black). The evolution of friction coefficient with time determined from inverse models (red) with the rate and state friction parameters shown. When the inverse model yields the result $b \neq 0$, the best fit with the constraint $b = 0$ is also shown (blue).

the step changes in velocity. If so, different values for $a - b$ would be expected for velocity-stepping and slide-hold-slide tests. That the $a - b$ values are consistent between the two types of tests and consistent with previous results indicates that we have accurately determined the steady-state velocity dependence of the CDZ gouge.

The estimates of D_c are variable (0–3.13 mm), and the estimate for the longest hold is particularly large (3.13 mm). The apparent large variation in D_c most likely reflects the high uncertainty in this parameter at very low b values. Previous studies also show very small to negligible values for b in phyllosilicate rich gouge (Saffer & Marone 2003; Moore & Lockner 2008; Ikari *et al.* 2009). Ikari *et al.* (2009) show that on average $b \approx 0$ in synthetic gouge composed of 50 per cent montomorillonite and 50 per cent quartz. For some velocity stepping tests they found small but non-zero values for b that span the same range of values (−0.0032 to 0.009) that we calculate for the CDZ gouge (−0.0014 to 0.0002). In addition, they find a similar range for $a - b$, and calculate large variation in D_c, which they attribute to high uncertainty.

The slide-hold-slide tests on dry gouge are generally best fit by the model parameters $b = 0$ and $0.0032 < a < 0.0040$, indicating that dry gouge is more rate-strengthening than brine-saturated gouge (Fig. 9). In two cases (H1 and H3) the magnitudes of b are predicted to be significantly greater than zero (0.002 and 0.005, respectively) resulting in $a - b$ values that are inconsistent with our other results on dry and saturated gouge. We attribute the results from these two tests to variability in strength, prior to or following the holds, that is not easily fit by a rate and state model; these tests can also be fairly well approximated using $b = 0$ (Fig. 9). Compared to brine-saturated gouge, the reloading behaviour of room-dry gouge is not as well fit by the rate and state friction model. Upon reloading the strength of the room-dry gouge is weaker than predicted by our model fits and appears similar to behaviour attributed to negative values of b in other clay-rich gouges, although in smectite the result is limited to higher velocities and lower normal stresses than investigated herein (Ikari *et al.* 2009). The inverse models allow for $b < 0$, as was the result for tests on saturated gouge, but this result was not the best fit for any of the room-dry gouge samples (Fig. 8).

We find that the correlation coefficient of a and b is very high for all tests (>0.95), which is a general consequence of using inverse models to determine rate and state friction parameters from experimental data (e.g. Reinen & Weeks 1992; Blanpied *et al.* 1998). As a result, there is greater uncertainty in each of these parameters independently than in their difference, $a - b$. Nevertheless, inverse models of 7 of 12 tests yield the result $b \approx 0$ and the other five tests can be qualitatively well fit with $b = 0$, providing confidence in this result.

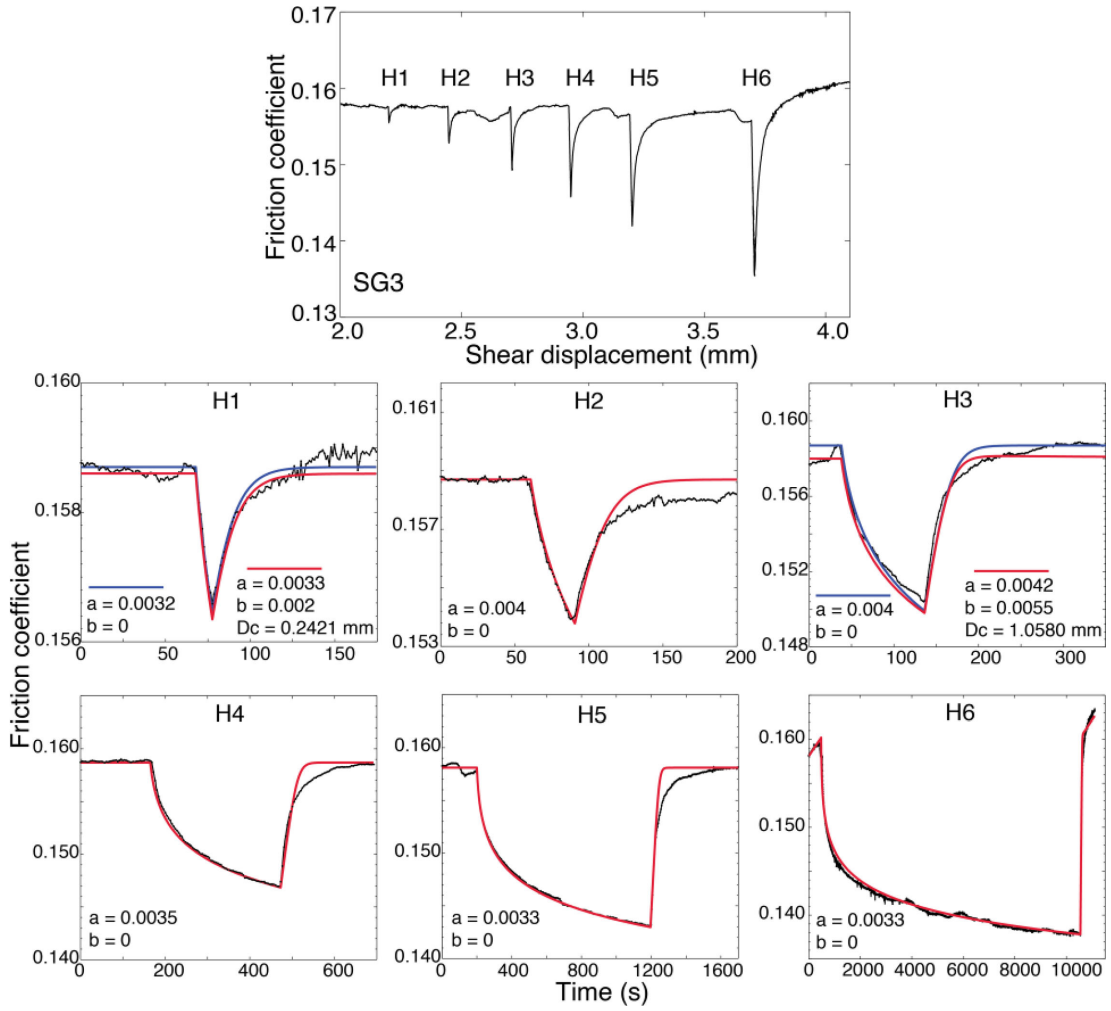

Figure 9. Top panel: an expanded view of the evolution of friction coefficient with displacement for the slide-hold-slide experiment SG3 also shown in Fig. 4. The sample is room-dry CDZ gouge deformed at 100 MPa effective normal stress, 100 °C and 0.6 μm s^{-1}. Bottom panels: the experimentally determined evolution of friction coefficient with time during the six holds (black). The evolution of friction coefficient with time determined from inverse models (red) with the rate and state friction parameters shown. When the inverse model yields the result $b \neq 0$, the best fit with the constraint $b = 0$ is also shown (blue).

3.4 Steady-state temperature dependence

The CDZ gouge is steady-state temperature weakening, $(aE_a - bE_b)/R > 0$ (eq. 2b), over the range of temperatures (80–120 °C) tested (Figs 4 and 10). The experimentally determined value of $(aE_a - bE_b)/R = 37.0$K (Fig. 10b). If the results from velocity-stepping and slide-hold-slide tests are taken into account ($a = 0.0014$, $b = 0$), then the activation energy is $E_a = 215$ kJ mol^{-1}.

The temperature-weakening frictional strength of the CDZ gouge is consistent with its velocity-strengthening behaviour if both the direct and evolution effects are governed by the same micromechanical processes, as has been shown in quartzofeldspathic gouge (Chester 1994; Blanpied *et al.* 1998). Previous studies on natural and synthetic phyllosilicate-rich fault gouges show that the effects of temperature on frictional strength depend on both the gouge composition and the range of conditions tested, largely because of the additional effects of adsorbed water (e.g. Moore *et al.* 1997; Morrow *et al.* 2000; Moore & Lockner 2004, 2008). In many cases temperature dependence is determined by conducting separate experiments at different temperatures rather than by using a temperature-stepping method. When separate experiments are conducted, differences in temperature must be large enough to dominate the sample-to-sample strength variation that may arise solely from differences in gouge structure. Results using this approach have shown both increasing and decreasing strength with increasing temperature (e.g. Moore *et al.* 1989, 1997; Moore & Lockner 2008; den Hartog and Spiers 2013). Illite strengthens as temperature is increased from 200 to 600 °C (Moore *et al.* 1989) and chrysotile serpentine weakens from 25 to 100 °C but then strengthens at temperatures higher than 100 °C as adsorbed water is removed (Moore *et al.* 1997). Differences between these prior results and the temperature weakening behaviour of the CDZ gouge documented herein are most likely related to the small range of temperature (80–120 °C) employed in the stepping tests. Both these results for the CDZ gouge and results for other phyllosilicate-rich gouge tested over larger temperature ranges consistently show, however, that when frictional strength decreases with increasing temperature the rate dependence is velocity strengthening. When strength increases with increasing temperature the rate dependence is either determined to be velocity-weakening or exhibits stick-slip behaviour, which is characteristic of velocity-weakening behaviour (Moore *et al.* 1989; Moore *et al.* 2004; Moore & Lockner 2008; den Hartog *et al.* 2012; den Hartog & Spiers 2013). All of these results are, therefore, consistent with the qualitative micromechanical model for temperature-dependent frictional strength set forth by Chester (1994).

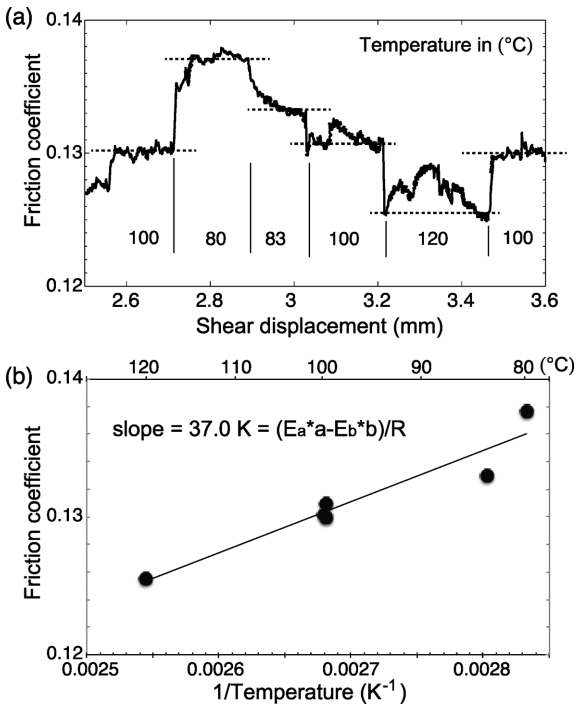

Figure 10. (a) The evolution of friction coefficient with shear displacement during the temperature-stepping part of the experiment (SG7) shown in Fig. 5(c). The experimental conditions are 100 MPa effective normal stress and 0.006 μm s^{-1} shear velocity. Temperature was stepped between 80, 100 and 120 °C. A furnace malfunction caused the temperature to slowly increase from 80 to 83 °C following one step, but the resulting strength is consistent with the temperature dependence determined from the other temperature steps. The CDZ gouge weakens with increasing temperature. (b) The change in friction coefficient with a change in $1/T$ provides a measure of the activation energies for the state and evolution effects (eq. 2b). Given $b = 0$ and $a = 0.0014$, $E_a = 215$ kJ.

4 DISCUSSION

4.1 Frictional behaviour of the SAFOD gouge

The coefficient of friction of the CDZ gouge (0.13 ± 0.01) is very close to the strength reported by Lockner *et al.* (2011) and Carpenter *et al.* (2012) at higher shear rates, and consensus is that the occurrence of the smectite mineral saponite in the CDZ gouge is responsible for the low coefficient of friction measured in this and previous studies. Phyllosilicate-rich gouges often have low coefficients of friction (μ < 0.5; Reinen *et al.* 1991, 1994; Moore *et al.* 1997; Saffer & Marone 2003; Moore & Lockner 2004, 2008; Moore & Rymer 2007; Ikari *et al.* 2009; Tembe *et al.* 2010), and smectite minerals, including saponite, are particularly weak (μ < 0.2; Logan & Rauenzahn 1987; Saffer & Marone 2003; Moore & Lockner 2004; Ikari *et al.* 2009; Tembe *et al.* 2010; Lockner *et al.* 2011; Carpenter *et al.* 2012). The weakness of smectite minerals, and therefore the CDZ gouge, is attributed to the low interlayer bond strength and, in the presence of pore fluid, structured adsorbed water layers that assist frictional sliding (Morrow *et al.* 2000).

The reduction in strength of the CDZ gouge under brine-saturated conditions compared to room-dry conditions is consistent with the qualitative observation from experiments on natural and simulated gouges of varying composition that water reduces frictional strength (Rutter & Mainprice 1978; Chester & Higgs 1992; Morrow *et al.* 2000; Moore & Lockner 2004; Ikari *et al.* 2007, 2009; Moore & Lockner 2008). Phyllosilicates with hydrophilic electrically charged surfaces, such as smectite, are shown to exhibit the greatest weakening when saturated, presumably because of the structured water films that form along grain surfaces (Summers & Byerlee 1977; Morrow *et al.* 2000). In addition to the difference in the magnitude of strength, we find that the magnitude of the rate-dependence in the CDZ gouge is two to three times greater under room-dry conditions. The effects of saturation state on strength and on its rate-dependence probably reflect the micro-mechanisms of deformation, which warrants further study. The *in situ* mechanical properties of the SAF in the vicinity of SAFOD, however, are best described by the dependence of velocity, temperature, and displacement on the strength of brine-saturated gouge.

4.2 Frictional strength of SAF at SAFOD

Velocity-strengthening behaviour of the CDZ gouge at the low velocities tested in this study is consistent with the aseismic, creeping behaviour of the central section of the SAF as also determined by Carpenter *et al.* (2012) and Lockner *et al.* (2011). The CDZ has the lowest frictional strength, by far, of all SAFOD materials tested (Tembe *et al.* 2006, 2009; Morrow *et al.* 2007; Carpenter *et al.* 2009), which is likely the reason that deformation is concentrated in this region of highly foliated gouge. The shear velocities employed herein, while slower than most friction studies, are faster than the shear rates seen along the SAF at SAFOD. The shear velocities used in this study (0.006–0.6 μm s^{-1}) correlate to a shear strain rate of 3.0×10^{-6} to 3.0×10^{-3} s^{-1} for a gouge layer thickness of 2 mm. Using the measured displacement rate of 21 mm yr^{-1} for the region near SAFOD (Titus *et al.* 2006) and the 4 m combined thickness of the SDZ (1.6 m) and CDZ (2.6 m) gouge zones, the shear strain rate for the SAF is 1.7×10^{-10} s^{-1}. Taking the base level coefficient of friction value of 0.135 at 0.6 μm s^{-1} (SG2), using the velocity dependence determined for the CDZ gouge ($a = a - b = 0.0014$), and substituting strain-rate for velocity in eqs (1a) and (1b) yields the result that the coefficient of friction along the creeping segment of the SAF is μ = 0.11 ± 0.01 at approximate *in situ* conditions. If the strain rate fluctuates as the result of laterally varying gouge thickness, or from the possible presence of additional creeping traces further east, the coefficient of friction could decrease further.

Measurements of stress orientations near the SAF have shown that the maximum horizontal compressive stress, S_H, is nearly normal to the SAF and the results of this study support the idea that slip along the SAF can occur with S_H at these orientations (Mount & Suppe 1987; Zoback *et al.* 1987; Provost & Houston 2001; Hickman & Zoback 2004). We use the results of these friction tests to calculate the approximate angle between the SAF and maximum horizontal compressive stress following the analysis of Tembe *et al.* (2009) and Lockner *et al.* (2011). Given the magnitude of the maximum and minimum horizontal effective principal compressive stress (126 and 51 MPa, respectively) determined by Hickman & Zoback (2004) in the SAFOD pilot hole, and using the coefficient of friction determined in this study calculated for the *in situ* strain rate (0.112), slip is permitted for angles between S_H and the plane of the SAF up to 79° (Fig. 11). Thus, at the depth of SAFOD, the CDZ is weak enough to permit slip along the creeping segment of the SAF without necessitating excess pore pressure.

The coefficient of friction determined for the SAFOD gouge is at the upper limit of the heat flow constraint. Brune *et al.* (1969) and Lachenbruch & Sass (1980) determined that the average shear strength of the SAF must be approximately 10 MPa based on the lack of a frictionally generated heat flow. Assuming a coefficient of

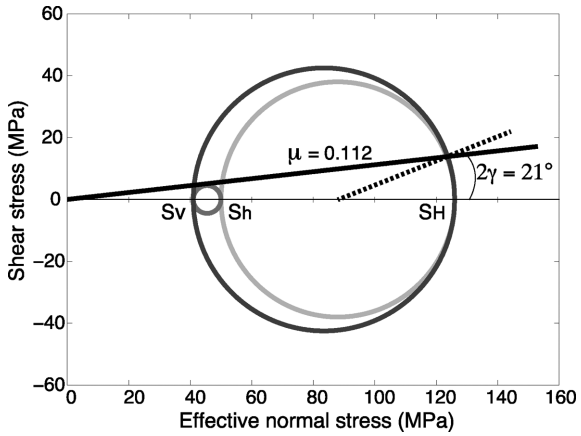

Figure 11. Mohr circle diagram depicting the effective principal stresses at SAFOD and the frictional failure envelope for the CDZ gouge at 100 °C and 10^{-10} s^{-1} ($\mu = 0.11$). Principle stresses were estimated from borehole geophysics conducted by Hickman & Zoback (2004) using data from the SAFOD pilot hole and are similar to the stress magnitudes used by Lockner *et al.* (2011). S_v, S_h and S_H indicate the vertical, minimum horizontal and maximum horizontal effective principle stresses, respectively. Pore fluid pressure is assumed to be hydrostatic at 2.7 km depth (27 MPa). Slip can occur within the CDZ if the maximum horizontal principal compressive stress is oriented equal to or greater than $90° - \gamma$ to the SAF plane. Based on the friction coefficient determined herein for *in situ* conditions, the angle between the SAF and the greatest compressive stress may be as low as 79.5° at this location and 2.7 km depth.

friction of 0.11 and an effective normal stress of 122 MPa (Lockner *et al.* 2011; Fig. 11), the shear stress at 2.7 km depth at SAFOD is 13.7 MPa. Our estimate of *in situ* friction is an extrapolation over 4 orders of magnitude in shear rate, so the possibility exists that at the lower shear rates or at higher temperatures different weakening mechanisms, such as dissolution-aided or dislocation-aided slip, may dominate the behaviour and produce even greater weakening of the SAFOD gouge than determined here.

5 CONCLUSIONS

(1) The CDZ gouge is extremely weak ($\mu < 0.13$) for shear at low laboratory rates and at *in situ* temperature (100 °C), effective normal stress (100 MPa), and pore fluid conditions present at SAFOD. When the laboratory relations are used to extrapolate to *in situ* strain rates, the coefficient of friction is 0.11 ± 0.01. The low coefficient of friction of the CDZ gouge at the depth range of SAFOD satisfies the apparent low frictional strength of the SAF based on heat flow and stress orientation measurements without calling on elevated pore fluid pressure.

(2) The CDZ gouge shows stable, rate-strengthening behaviour ($a - b = 0.0014 \pm 0.0005$) at the conditions and rates tested. Rate-strengthening behaviour is consistent with aseismic creep on the SAF at SAFOD and the magnitude of the steady-state rate dependence is similar to that previously reported by Lockner *et al.* (2011) and Carpenter *et al.* (2012) at higher velocities.

(3) The CDZ gouge exhibits negligible state-dependence ($b \approx 0$), which results in negligible time-dependent healing and transient strength.

(4) Temperature-weakening behaviour is observed for the CDZ gouge. This is consistent with rate-strengthening behaviour where the micromechanisms that cause the temperature and rate dependencies are the same, and described by an activation energy of 215 kJ mol^{-1}.

ACKNOWLEDGEMENTS

This research was supported by the NSF EarthScope program (EAR-0643339), and the Southern California Earthquake Center. SCEC is funded by NSF Cooperative Agreement EAR-1033462 and USGS Cooperative Agreement G12AC20038. The SCEC contribution number for this paper is 1942. We thank Clayton Powell for assistance in the laboratory, and Diane Moore and Brett Carpenter for helpful reviews of the manuscript.

REFERENCES

Blanpied, M.L., Tullis, T.E. & Weeks, J.D., 1998. Effects of slip, slip rate, and shear heating on the friction of granite, *J. geophys. Res.,* **103**(B1), 489–511.

Bos, B., Peach, C.J. & Spiers, C.J., 2000. Frictional-viscous flow of simulated fault gouge caused by the combined effects of phyllosilicates and pressure solution, *Tectonophysics,* **327,** 173–194.

Boulton, C., Moore, D.E., Lockner, D.A., Toy, V.G., Townend, J. & Sutherland, R., 2014. Frictional properties of exhumed fault gouges in DFDP-1 cores, Alpine Fault, New Zealand, *Geophys. Res. Lett.,* **41,** doi:10.1002/2013GL058236.

Boulton, C., Carpenter, B.M., Toy, V. & Marone, C., 2012. Physical properties of surface outcrop cataclastic fault rocks, Alpine Fault, New Zealand, *Geochem. Geophys. Geosyst.,* **13**(1), doi:10.1029/2011GC003872.

Bradbury, K.K., Evans, J.P., Chester, J.S., Chester, F.M. & Kirschner, D.L., 2011. Lithology and internal structure of the San Andreas Fault at depth based on characterization of phase 3 whole-rock core in the San Andreas Fault Observatory at Depth (SAFOD) borehole, *Earth planet. Sc. Lett.,* **310**(1–2), 131–144.

Brune, J.N., Henyey, T.L. & Roy, R.F., 1969. Heat flow, stress, and rate of slip along San Adreas Fault, California, *J. geophys. Res.,* **74,** 3821–3827.

Carpenter, B.M., Marone, C. & Saffer, D.M., 2009. Frictional behavior of materials in the 3D SAFOD volume, *Geophys. Res. Lett.,* **36,** L05302, doi:10.1029/2008GL036660.

Carpenter, B.M., Marone, C. & Saffer, D.M., 2011. Weakness of the San Andreas Fault revealed by samples from the active fault zone, *Nat. Geosci.,* **4**(4), 251–254.

Carpenter, B.M., Saffer, D.M. & Marone, C., 2012. Frictional properties and sliding stability of the San Andreas Fault from deep drill core, *Geology,* **40**(8), 759–762.

Chester, F.M., 1988. The brittle-ductile transition in a deformation-mechanism map for halite, *Tectonophysics,* **154,** 125–136.

Chester, F.M., 1994. Effects of temperature on friction: constitutive-equations and experiments with quartz gouge, *J. geophys. Res.,* **99**(B4), 7247–7261.

Chester, F. & Higgs, N., 1992. Multimechanism friction constitutive model for ultrafine quartz gouge at hypocentral conditions, *J. geophys. Res.,* **97**(B2), 1859–1870.

Chester, J.S. *et al.*, 2007. Deformation of sedimentary rock across the San Andreas fault zone; mesoscale and microscale structures displayed in core from SAFOD, *EOS, Trans. Am. geophys. Un.,* **88**(52), Suppl., Abstract T42C-05.

Coble, C.G., 2010. Frictional strength of the creeping segment of the San Andreas Fault, *MS thesis,* 63 pp., Texas A&M University, College Station, TX.

Collettini, C., Niemeijer, A., Viti, C. & Marone, C., 2009. Fault zone fabric and fault weakness, *Nature,* **462,** 907–910.

den Hartog, S.A.M. & Spiers, C.J., 2013. Influence of subduction zone conditions and gouge composition on frictional slip stability of megathrust faults, *Tectonophysics,* **600,** 75–90.

den Hartog, S.A.M., Peach, C.J., de Winter, D.A.M., Spiers, C.J. & Shimamoto, T., 2012. Frictional properties of megathrust fault gouges at low sliding velocities: new data on effects of normal stress and temperature, *J. Struct. Geol.,* **38,** 156–171.

Dieterich, J.H., 1978. Time dependent friction and the mechanics of stick-slip, *Pure appl. Geophys.,* **116,** 790–806.

Faulkner, D.R. & Rutter, E.H., 2003. The effect of temperature, the nature of the pore fluid, and subyield differential stress on the permeability off phyllosilicate-rich fault gouge, *J. geophys. Res.,* **108**(B5), 2227, doi:10.1029/2001JB001581.

French, M.E., Kitajima, H., Chester, J.S., Chester, F.M. & Hirose, T., 2014. Displacement and dynamic weakening processes in smectite-rich gouge from the central deforming zone of the San Andreas Fault, *J. geophys. Res.,* **119,** 1777–1802.

Fulton, P.M. & Saffer, D.M., 2009a. Effect of thermal refraction on heat flow near the San Andreas Fault, Parkfield, California, *J. geophys. Res.,* **114,** B06408, doi:10.1029/2008JB005796.

Fulton, P.M. & Saffer, D.M., 2009b. Potential role of mantle-derived fluids in weakening the San Andreas Fault, *J. geophys. Res.,* **114,** B07408, doi:10.1029/2008JB006087.

Fulton, P.M., Saffer, D.M., Harris, R.N. & Bekins, B.A., 2004. Re-evaluation of heat flow data near Parkfield, CA: evidence for a weak San Andreas Fault, *Geophys. Res. Lett.,* **31,** L15S15, doi:10.1029/2003GL019378.

Fulton, P.M., Saffer, D.M. & Bekins, B.A., 2009. A critical evaluation of crustal dehydration as the cause of an overpressured and weak San Andreas Fault, *Earth planet. Sc. Lett.,* **284**(3–4), 447–454.

Gratier, J.P., Richard, J., Renard, F., Mittempergher, S., Doan, M.L., Di Toro, G., Hadizadeh, J. & Boullier, A.M., 2011. Aseismic sliding of active faults by pressure solution creep: evidence from the San Andreas Fault Observatory at depth, *Geology,* **39**(12), 1131–1134.

Hadizadeh, J., Mittempergher, S., Gratier, J.-P., Renard, F., Di Toro, G., Richard, J. & Babaie, H.A., 2012. A microstructural study of fault rocks from the SAFOD: Implications for the deformation mechanisms and strength of the creeping segment of the San Andreas Fault, *J. Struct. Geol.,* **42,** 246–260.

Heard, H.C., 1963. Effect of large changes in strain rate in the experimental deformation of Yule Marble, *J. Geol.,* **71,** 162–195.

Hickman, S. & Zoback, M., 2004. Stress orientations and magnitudes in the SAFOD pilot hole, *Geophys. Res. Lett.,* **31,** L15S12, doi:10.1029/2004GL020043.

Holdsworth, R.E., van Diggelen, E.W.E., Spiers, C.J., de Bresser, J.H.P., Walker, R.J. & Bowen, L., 2011. Fault rocks from the SAFOD core samples: implications for weakening at shallow depths along the San Andreas Fault, California, *J. Struct. Geol.,* **33**(2), 132–144.

Ikari, M.J., Saffer, D.M. & Marone, C., 2007. Effect of hydration state on the frictional properties of montmorillonite-based fault gouge, *J. geophys. Res.,* **112,** B06423, doi:10.1029/2006JB004748.

Ikari, M.J., Saffer, D.M. & Marone, C., 2009. Frictional and hydrologic properties of clay-rich fault gouge, *J. geophys. Res.,* **114,** B05409, doi:10.1029/2008JB006089.

Lachenbruch, A.H., 1980. Frictional heating, fluid pressure, and the resistance to fault motion, *J. geophys. Res.,* **85,** 6097–6112.

Lachenbruch, A.H. & Sass, J.H., 1980. Heat-flow and energetics of the San-Andreas fault zone, *J. geophys. Res.,* **85,** 6185–6222.

Lockner, D.A., Morrow, C., Moore, D. & Hickman, S., 2011. Low strength of deep San Andreas Fault gouge from SAFOD core, *Nature,* **472**(7341), 82–85.

Logan, J.M. & Rauenzahn, K.A., 1987. Frictional dependence of gouge mixtures of quartz and montmorillonite on velocity, composition, and fabric, *Tectonophysics,* **144**(1–3), 87–108.

Mizoguchi, K., Hirose, T., Shimamoto, T. & Fukuyama, E., 2009. High-velocity frictional behavior and microstructure evolution of fault gouge obtained from Hojima fault, southwest Japan, *Tectonophysics,* **471,** 285–296.

Moore, D.E. & Lockner, D.A., 2004. Crystallographic controls on the frictional behavior of dry and water-saturated sheet structure minerals, *J. geophys. Res.,* **109,** B03401, doi:10.1029/2003JB002582.

Moore, D.E. & Lockner, D.A., 2008. Talc friction in the temperature range 25°–400 °C: Relevance for fault-zone weakening, *Tectonophysics,* **449,** 120–132.

Moore, D.E. & Lockner, D.A., 2011. Frictional strengths of talc-serpentine and talc-quartz mixtures, *J. geophys. Res.,* **116,** B01403, doi:10.1029/2010JB007881.

Moore, D.E. & Lockner, D.A., 2013. Chemical controls on fault behavior; weakening of serpentinite sheared against quartz-bearing rocks and its significance for fault creep in the San Andreas system, *J. geophys. Res.,* **118**(B5), 2558–2570.

Moore, D.E. & Rymer, M.J., 2007. Talc-bearing serpentinite and the creeping section of the San Andreas Fault, *Nature,* **448,** 795–797.

Moore, D.E., Lockner, D.A., Tanaka, H. & Iwata, K., 2004. The coefficient of friction of chrysotile gouge at seismogenic depths, *Int. Geol. Rev.,* **46**(5), 385–398.

Morrow, C.A., Shi, L.Q. & Byerlee, J.D., 1984. Permeability of fault gouge under confining pressure and shear stress, *J. geophys. Res.,* **89**(B5), 3193–3200.

Moore, D.E., Summers, R. & Byerlee, J.D., 1989. Sliding behavior and deformation textures of heated illite gouge, *J. Struct. Geol.,* **11,** 329–342.

Moore, D.E., Lockner, D.A., Ma, S., Summers, R. & Byerlee, J.D., 1997. Strengths of serpentinite gouges at elevated temperatures, *J. geophys. Res.,* **102,** 14 787–14 801.

Morrow, C.A., Moore, D.E. & Lockner, D.A., 2000. The effect of mineral bond strength and adsorbed water on fault gouge frictional strength, *Geophys. Res. Lett.,* **27,** 815–818.

Morrow, C.A., Solum, J., Tembe, S., Lockner, D.A. & Wong, T.-f., 2007. Using drill cutting separates to estimate the strength of narrow shear zones at SAFOD, *Geophys. Res. Lett.,* **34,** L11301, doi:10.1029/2007GL029665.

Mount, V.S. & Suppe, J., 1987. State of stress near the San Andreas Fault: implications for wrench tectonics, *Geology,* **15,** 1143–1146.

Niemeijer, A., Marone, C. & Elsworth, D., 2010. Fabric induced weakness of tectonic faults, *Geophys. Res. Lett.,* **37,** L03304, doi:10.1029/2009GL041689.

Numelin, T., Marone, C. & Kirby, E., 2007. Frictional properties of natural fault gouge from a low angle normal fault, Panamint Valley, California, *Tectonics,* **26,** TC2004, doi:10.1029/2005TC001916.

Provost, A.S. & Houston, H., 2001. Orientation of the stress field surrounding the creeping section of the San Andreas Fault: evidence for a narrow mechanically weak fault zone, *J. geophys. Res.,* **106,** 11 373–11 386.

Reinen, L.A. & Weeks, J.D., 1992. Determination of rock friction constitutive parameters using an iterative least squares inversion method, *J. geophys. Res.,* **98**(B9), 15 937–15 950.

Reinen, L.A., Weeks, J.D. & Tullis, T.E., 1991. The frictional behavior of serpentinite: implications for aseismic creep on shallow crustal faults, *Geophys. Res. Lett.,* **18,** 1921–1924.

Reinen, L.A., Weeks, J.D. & Tullis, T.E., 1994. Ther frictional behavior of lizardite and antigorite serpentinites: experiments, constitutive models, and implications for natural faults, *Pure appl. Geophys.,* **143,** 317–358.

Rice, J.R., 1992. Fault stress states, pore pressure distributions, and the weakness of the San Andreas Fault, in *Fault Mechanics and Transport Properties of Rocks,* pp. 475–504, eds Evans, B. & Wong, T.-f., Academic Press.

Rutter, E.H. & Mainprice, D.H., 1978. Effect of water on stress relaxation of faulted and un-faulted sandstone, *Pure appl. Geophys.,* **116,** 634–654.

Saffer, D.M. & Marone, C., 2003. Comparison of smectite- and illite-rich gouge frictional properties: application to the updip limit of the seismogenic zone along subduction megathrusts, *Earth planet. Sci. Lett.,* **215,** 219–235.

Schleicher, A.M., van der Pluijm, B.A. & Warr, L.N., 2010. Nanocoatings of clay and creep of the San Andreas Fault at Parkfield, California, *Geology,* **38,** 667–670.

Smith, S.A.F. & Faulkner, D.R., 2010. Laboratory measurements of the frictional properties of the Zuccale low-angle normal fault, Elba Island, Italy, *J. geophys. Res.,* **115,** B02407, doi:10.1029/2008JB006274.

Sone, H. & Shimamoto, T., 2009. Frictional resistance of faults during accelerating and decelerating earthquake slip, *Nature,* **2,** 705–708.

Summers, R. & Byerlee, J., 1977. A note on the effect of fault gouge composition on the stability of frictional sliding, *Int. J. Rock Mech. Min. Sci.,* **14**(3), 155–160.

Takahashi, M., Mizoguchi, K., Kitamura, K. & Masuda, K., 2007. Effects of clay content on the frictional strength and fluid transport property faults, *J. geophys. Res.,* **112**(B8), doi:10.1029/2006JB004678.

Tembe, S., Lockner, D.A., Solum, J.G., Morrow, C.A., Wong, T.-f. & Moore, D.E., 2006. Frictional strength of cuttings and core from SAFOD drillhole phases 1 and 2, *Geophys. Res. Lett.,* **33,** L23307, doi:10.1029/2006GL027626.

Tembe, S., Lockner, D.A. & Wong, T.-f., 2009. Constraints on the stress state of the San Andreas Fault with analysis based on core and cuttings from San Andreas Fault Observatory at Depth (SAFOD) drilling phases 1 and 2, *J. geophys. Res.,* **114,** B11401, doi:10.1029/2008JB005883.

Tembe, S., Lockner, D.A. & Wong, T.-f., 2010. Effect of clay content and mineralogy on frictional sliding behavior of simulated gouges: binary and ternary mixtures of quartz, illite, and montmorillonite, *J. geophys. Res.,* **115,** B03416, doi:10.1029/2009JB006383.

Titus, S.J., DeMets, C. & Tikoff, B., 2006. Thirty-five-year creep rates for the creeping segment of the San Andreas Fault and the effects of the 2004 Parkfield earthquake: constraints from alignment arrays, continuous global positioning system, and creepmeters, *Bull. seism. Soc. Am.,* **96,** S250–S268.

Williams, C.F., Grubb, F.V. & Galanis, S.P. Jr., 2004. Heat flow in the SAFOD pilot hole and implications for the strength of the San Andreas Fault, *Geophys. Res. Lett.,* **31,** L15S14, doi:10.1029/2003GL019352.

Zoback, M., Hickman, S. & Ellsworth, W., 2010. Scientific drilling into the San Andreas Fault Zone, *EOS, Trans. Am. geophys. Un.,* **91,** 197–204.

Zoback, M.D. *et al.*, 1987. New evidence on the state of stress of the San Andreas Fault system, *Science,* **238,** 1105–1111.